

COMMON RESEARCH MODELS FOR SMALL UNCREWED AERIAL VEHICLES

Juan Rasines Mazo[1], Ben Van Magill[1] & Dries Verstraete[1]

[1]School of Aerospace, Mechanical and Mechatronic Engineering, The University of Sydney, Australia

Abstract

At chord Reynolds numbers of 150,000 to 300,000, laminar separation bubbles govern the aerodynamic behaviour of small fixed-wing UAVs. Simulation tools for this regime lack a common validation reference. Each group tests against its own platform, which makes cross-institutional comparison impossible. Two common research models are proposed to address this gap: a flying-wing and a V-tailed configuration. Both are below 1 kg take-off mass, and characterised in the wind tunnel over a range of angles of attack and sideslip angles at airspeeds between 15 and 25 m/s. The reflexed camber required to generate longitudinal stability without a dedicated tail surface reduces the flying-wing maximum lift coefficient to 0.63, compared to 1.05 for the tailed configuration. The higher aspect ratio and unconstrained airfoil camber of the conventional tailed configuration give it a 31 % higher maximum lift-to-drag ratio. Both configurations exhibit Reynolds-number-dependent stability margins. The flying-wing static margin increases from 3.1% to 6.1% MAC while the V-tailed aircraft's static margin decreases from 3.5 % to 2.3 % MAC across the tested speed range. Lateral static stability shows strong Reynolds-number sensitivity for the V-tail but is almost Reynolds-independent for the flying-wing configuration. This difference is likely governed by fin chord Reynolds number and laminar separation bubble behaviour on the fin surface. The geometry and full experimental dataset for both reference models are made publicly available as a shared reference for systematic validation of low-, mid-, and high-fidelity aerodynamic methods in this regime.

Keywords: Uncrewed Aerial Vehicles, common research model, small aircraft, experimental, validation

1. Introduction

Aerodynamics validation of transport aircraft is widespread because the aeronautics field has agreed on common research models. The tools used to design transport aircraft have been tested against a small set of openly shared benchmark geometries: the ONERA M6 transonic wing [1], the DLR-F4 configuration, and the NASA Common Research Model [2, 3]. Any group claiming an improved turbulence closure model or a more accurate solver has been measured against results computed by other institutions for the same geometry. The same principle has since been applied to distributed electric propulsion platforms [4] and international aero-elastic tailoring programs [5, 6], enabling cross-institutional validation that would otherwise be impossible [7, 8].

The aerodynamics of small Uncrewed Aerial Vehicles (UAVs) has not reached that agreement. At chord Reynolds numbers between 10^4 and 10^5, small UAV flows are governed by laminar separation bubbles, viscous-dominated pressure recovery, and flow transition phenomena that conventional turbulence closures handle poorly [9, 10, 11]. The accuracy of any simulation tool in this regime depends on modelling choices, including transition criteria, bubble representation, and near-wall resolution. These choices vary between groups and produce substantially different predictions for nominally the same case [12]. Without a shared geometry and a common experimental dataset, it is not possible to determine whether disagreement between simulation results reflects a physical modelling difference or simply a platform difference. Validation remains confined to individual institutions and individual aircraft.

Prior work has established isolated experimental datasets for specific small UAV platforms. Wind tunnel and flight testing of the Ultra Stick 25e and Ultra Stick 120 provided longitudinal and lateral dynamic models using frequency-domain system identification [13, 14]. The Skywalker X8 flying wing has similarly been characterised, including a full aerodynamic coefficient set and linearised state-space representations [15, 16]. However, without a common geometry, a discrepancy between a measured and a predicted coefficient cannot be attributed solely to solver error. It may also reflect a platform-specific flow feature absent from the model. The comparison cannot be made. Incomplete geometric documentation compounds this, as does the discontinuation of several of the tested vehicles. As a consequence, the community has individual calibration points, not a shared reference.

Two common research models for small fixed-wing UAVs with a take-off mass below 1 kg, as presented in this work, fill this gap, with the experimental dataset made publicly available for simulation validation.[1] The two configurations cover the two most common stability architectures in this vehicle class. In the flying-wing, the wing must carry both lift and pitch stability, whereas these functions are decoupled for the V-tailed design. Together they also bracket the practical aspect ratio range for sub-1 kg fixed-wing UAVs and enable structured benchmarking at the Reynolds numbers where laminar separation bubbles, flow transition, and viscous pressure recovery govern aerodynamic behaviour [9, 10].
The remainder of the paper is organised as follows. Section 2. describes the two CRM geometries, their physical basis, and the wind tunnel experimental setup. Section 3. presents the aerodynamic polars and compares the performance of the two configurations, with particular attention to the Reynolds-number dependence of the drag polar and lift curve. Section 4. characterises the static stability derivatives of both configurations across the tested speed range and discusses the implications of their Reynolds-number sensitivity for simulation validation. Section 5. draws conclusions and identifies priority directions for extending the dataset.

2. Geometry and Experimental Setup

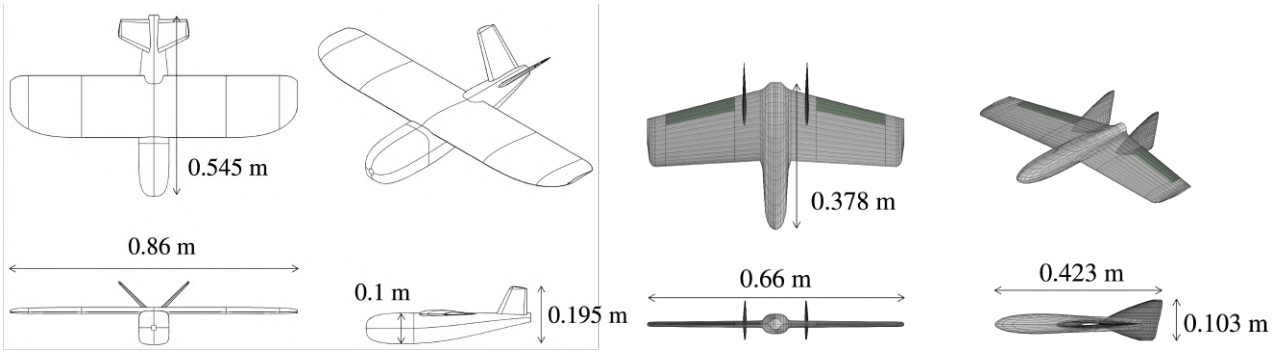
The two configurations were selected to represent the stability architectures that define opposite ends of the sub-1 kg fixed-wing design space. In the flying-wing configuration (CRM 2: NG), the wing must generate both lift and a restoring pitching moment. This constrains the airfoil to a reflexed camber line and imposes a direct penalty on maximum lift. In the V-tailed configuration (CRM 1: NT), a separate tail surface provides pitch stability which frees up the wing camber for lift optimisation. The difference is not just geometric, it is a fundamental trade between aerodynamic efficiency and configuration simplicity that governs how each vehicle responds to Reynolds-number-dependent flow phenomena. The two CRMs therefore stress-test simulation tools against qualitatively different aerodynamic problems within the same Reynolds number regime. Their wing loadings are close enough (47.3 and 44.2 N/m^2) to isolate configuration effects from wing loading effects in comparative studies.

2.1 Flying-Wing and V-Tail Configuration

The following section presents the geometric definition of the two proposed common research models, for which a summary of the key physical properties is presented in Table 1. The NT CRM is a conventional high-wing configuration with a V-tail (see Figure 1a), loosely based on the Nano Talon FPV model. It has conventional wing ailerons and all-movable V-tail control surfaces. The second CRM has a forward-swept flying-wing configuration with twin vertical tails (see Figure 1b), as seen in the popular Nano Goblin and Nano Gremlin FPV (first-person view) plank designs. It has elevon control surfaces (combined aileron and elevator controls) and the vertical tails are fixed. These two configurations represent a wide variety of typical fixed-wing designs with electric propulsion for the small UAV class. Experimental testing of the two proposed CRM vehicles was conducted to create an initial database of results and facilitate adoption by the research community. The following subsections summarise the relevant aerodynamic and static stability properties of the CRMs, as evaluated

[1] The CRM geometry and wind tunnel results can be found at:
https://github.com/juanrasinesmazo/SmallUAVCommonResearchModels

from wind tunnel tests. It is noted that only a subset of the complete wind tunnel test results is presented in this work; the full dataset is available with the geometry models for both CRMs.



(a) CRM 1: NT (b) CRM 2: NG

Figure 1 – Three-view drawing of the two common research model (CRM) geometries.

Table 1 – Summary of key geometric properties for both CRMs.

Description	Parameter	NT	NG	Unit
Maximum Take-off Mass	m_{TO}	0.710	0.509	kg
Wing-loading	W/S	47.3	44.2	N/m^2
Mean Aerodynamic Chord	MAC	0.159	0.193	m
Wing Area	S	0.148	0.113	m^2
Wing Span	b	0.86	0.66	m
Aspect Ratio	AR	5.00	3.85	–

2.2 Wind Tunnel Setup and Measurement Repeatability

A wind tunnel test campaign was performed in the 4x3-foot low-speed wind tunnel at the University of Sydney. To-scale wind tunnel models of the two CRM geometries were mounted on an articulated sting mount, as shown in Figure 2.



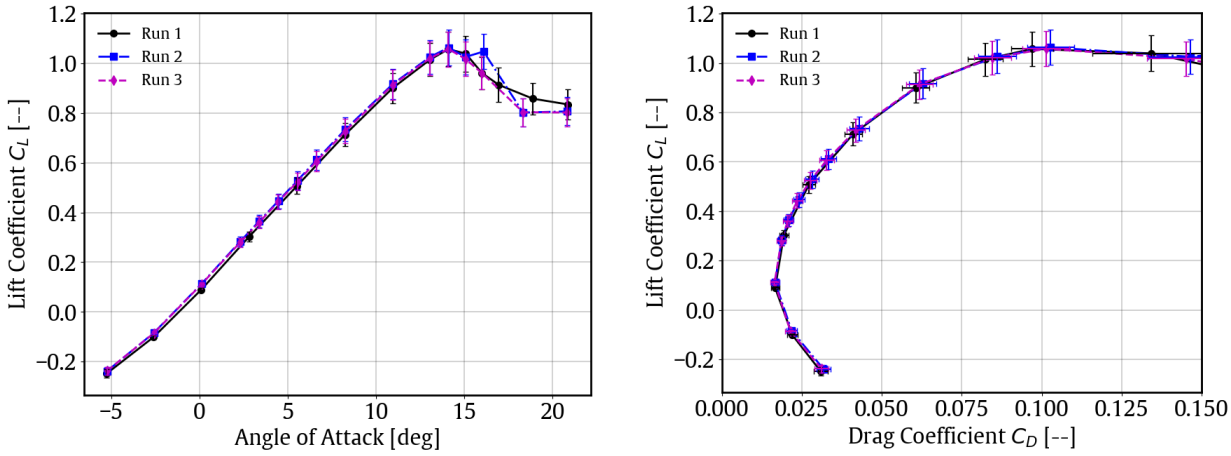
(a) NT (b) NG

Figure 2 – Wind tunnel models for both CRM geometries mounted inside the 4x3-foot low-speed wind tunnel test section.

Angle of attack and sideslip sweeps at various airspeeds (15 – 25 m/s) were performed to measure the steady-state (static) forces and moments. The models were mounted directly to a six-component

precision loadcell, namely the ATI Nano25, at their respective centres of gravity, and the analog signals were digitised with a LabJack Data Acquisition (DAQ) board. The selected test velocity ranges correspond to Reynolds number ranges of 187,000–312,000 and 227,000–379,000 for the NT and NG CRMs, respectively. The effects of solid and wake blockage were accounted for following the methodology in ref. [17]. The solid blockage for the full-scale wind tunnel models was satisfactorily small, being 0.4 % and 0.2 % for the NT and NG CRMs, respectively. Similarly, the turbulence intensity of the wind tunnel was low, with experimentally measured values below 0.3 % for the test velocities [18]. Each test condition was sampled at 1000 Hz over 10 s, and the mean and standard deviations of all force and moment measurements were calculated. A covariance matrix, assuming independent measurement channels (no cross-covariances), was constructed and used to propagate errors in the post-processing evaluation of aerodynamic coefficients and derivatives [19].

An initial study of wind tunnel variability was conducted by testing the NT CRM at 20 m/s. Three identical angle of attack sweeps were performed across three independent runs on two different test days, with differences in atmospheric air temperature and humidity. Additional out-of-sample angle of attack conditions were also evaluated for Runs 2 and 3. Figure 3 presents the corresponding results for both the lift coefficient trend with angle of attack and the drag coefficient. Results show near-identical mean lift and drag coefficient values across the linear portion of the angle of attack range. Standard deviation magnitudes likewise agree well between the three different runs. The post-stall results show greater deviation between re-runs due to partially and eventually fully separated flow behaviour over the wing geometry. Despite this, the mean values of the three runs are still within error bounds of each other. The measured drag values are aslo highly consistent across the entire drag polar, which provides additional confidence in the repeatability of the experiment.



(a) Lift coefficient vs. angle of attack

(b) Lift vs. drag coefficient

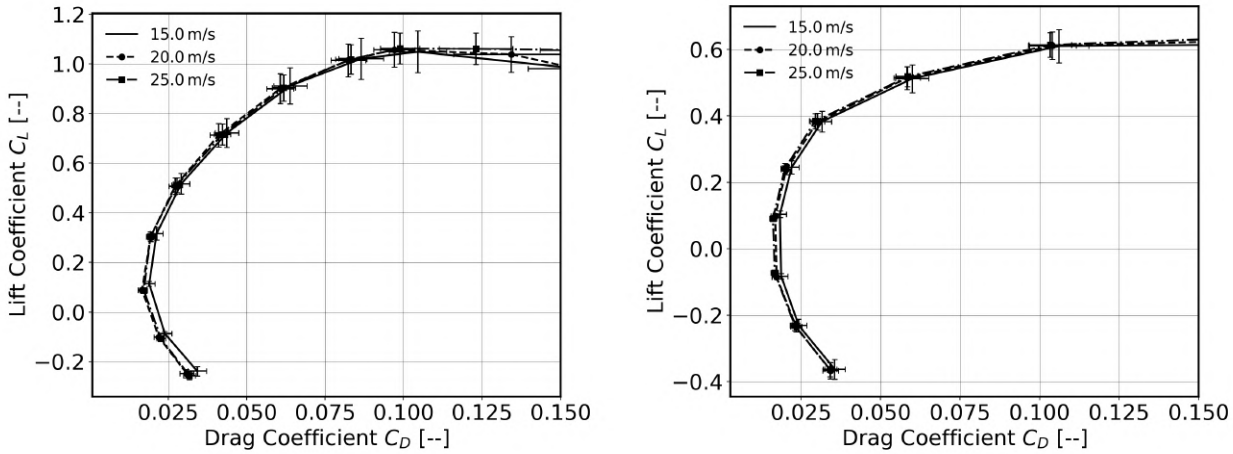
Figure 3 – Variability of experimental aerodynamic results for the NT CRM at 20 m/s from wind tunnel testing of three independent runs across different test days.

3. Reynolds-Number-Dependent Performance For Both Configurations

The following section presents the key aerodynamic behaviour characterised for the two CRMs through wind tunnel testing. The lift-drag polars at three airspeeds (15, 20, and 25 m/s) and zero sideslip conditions are shown in Figure 4 for both CRMs. Similarly, the lift-to-drag trends with lift coefficient are shown in Figure 5 for equivalent conditions. A summary of the key aerodynamic parameters is presented in Table 2, including the maximum lift coefficient $C_{L_{\max}}$, the maximum lift-to-drag ratio $L/D_{\max}$, and the minimum drag coefficient $C_{D_{\min}}$. The flying-wing configuration must generate pitch stability through reflexed camber, which constrains the wing to a geometry that penalises maximum lift compared to a design optimised for lift alone. The tailed configuration, on the other hand, offloads pitch stability to a separate surface, so each surface can be optimised independently. The

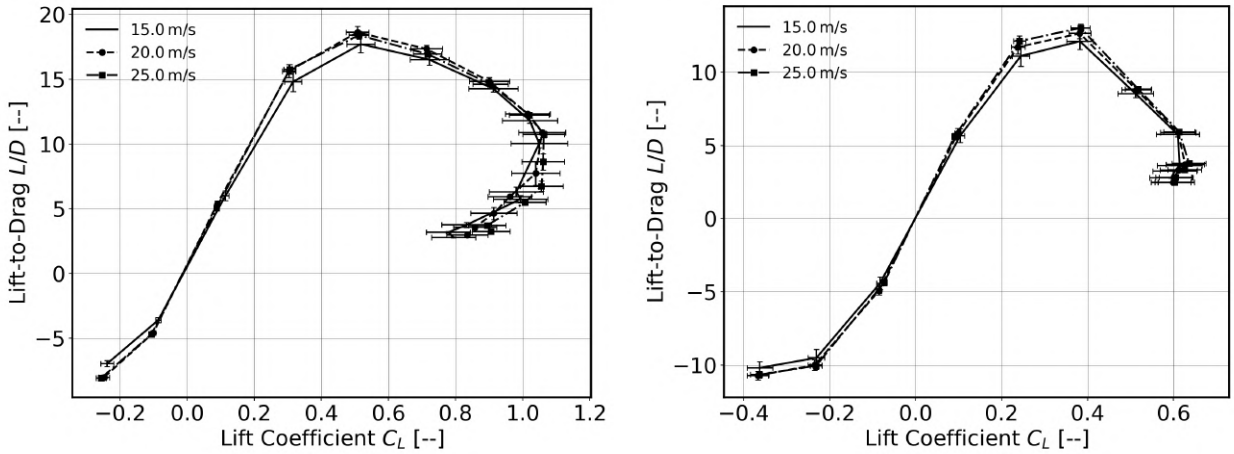
aerodynamic cost of that constraint is quantified below.

Both CRMs demonstrate a reduction in $C_{D_{\text{min}}}$ with increasing airspeed across the tested Reynolds number range. This behaviour is consistent with the Re-dependent character of laminar separation bubbles at these flow conditions [12, 13]. As Re increases, the adverse pressure gradient required to trigger turbulent reattachment is reached earlier on the surface, shortening the bubble and reducing the associated form drag contribution to $C_{D_{\text{min}}}$. For the NT, $C_{D_{\text{min}}}$ decreases from 0.0190 at 15 m/s to 0.0167 at 20 m/s and plateaus at higher airspeeds, indicating the bubble has reached a minimum stable length within the tested Reynolds number range. The NG shows no equivalent plateau, with $C_{D_{\text{min}}}$ decreasing from 0.0184 at 15 m/s to 0.0162 at 25 m/s, suggesting that the minimum drag condition lies outside the tested envelope.



(a) NT (b) NG

Figure 4 – Lift vs. drag coefficient polars at various airspeeds for both CRMs.



(a) NT (b) NG

Figure 5 – Lift-to-drag vs. lift coefficient at various airspeeds for both CRMs.

The lift coefficient rolls off smoothly beyond the maximum rather than showing an abrupt break. The gradual stall behaviour is similar between the NT and NG configurations, and the polar shape near $C_{L_{\text{max}}}$ does not vary with airspeed. This stall behaviour indicates progressive separation and is consistent with the low-Re regime. The absence of a sharp stall break and its Re-independence within the tested range are relevant benchmarks for simulation tool validation: tools predicting an abrupt C_L drop at stall for these geometries should be considered inconsistent with the experimental

evidence. The NT CRM has a maximum lift coefficient of approximately $C_{L_{\max}} = 1.05$ across the tested airspeeds, 66 % higher than that of the NG CRM. The reduction in maximum lift coefficient stems from the reflexed camber line required to generate a positive zero-lift pitching moment in the flying wing configuration.

Maximum range for an electrically propelled aircraft scales with L/D, which is maximised at the operating condition where profile drag and induced drag contribute equally to total drag. Any deviation towards lower or higher lift coefficients increases one component faster than it reduces the other, and the optimal lift coefficient $C_{L_{\text{opt}}} = \sqrt{C_{D0}/k}$ defines this balance, where k is the induced drag factor. For a given span efficiency, k scales inversely with aspect ratio, so the NG's lower AR of 3.85 compared to 5.0 for the NT raises k by approximately 30 %. This increases induced drag at the optimal operating point. The NG's $C_{D_{\min}}$ is marginally lower than the NT (by approximately 5 drag counts), reducing profile drag by roughly 3 %. This benefit is insufficient to offset the induced drag penalty. The net result is a maximum lift-to-drag ratio of 12.5 for the NG compared to 18.0 for the NT, a 31 % endurance penalty that the $C_{D_{\min}}$ advantage cannot recover.

Table 2 – Summary of the aerodynamic performance parameters for both CRMs at various airspeeds. Standard deviations for experimental results are presented in-line as (±).

CRM	V [m/s]	$C_{L_{\max}}$	$L/D_{\max}$	$C_{D_{\min}}$
NT	15.0	1.05 (±0.084)	17.72 (±0.66)	0.0190 (±0.0019)
	17.5	1.05 (±0.077)	18.13 (±0.53)	0.0174 (±0.0015)
	20.0	1.06 (±0.070)	18.63 (±0.45)	0.0167 (±0.0013)
	22.5	1.06 (±0.065)	18.49 (±0.35)	0.0170 (±0.0012)
	25.0	1.06 (±0.062)	18.41 (±0.30)	0.0173 (±0.0011)
NG	15.0	0.61 (±0.052)	12.11 (±0.55)	0.0184 (±0.0020)
	17.5	0.62 (±0.047)	12.51 (±0.44)	0.0170 (±0.0016)
	20.0	0.63 (±0.044)	12.54 (±0.34)	0.0169 (±0.0014)
	22.5	0.63 (±0.042)	12.85 (±0.30)	0.0164 (±0.0013)
	25.0	0.64 (±0.040)	13.02 (±0.26)	0.0162 (±0.0011)

4. Static Stability

Both CRMs exhibit static stability margins that vary measurably with Reynolds number, with the NT and NG showing opposing trends in longitudinal stability across the tested speed range. The key longitudinal-directional parameters are summarised in Table 3 including the lift-curve and pitch-curve slopes (C_{L_α} and C_{m_α}, respectively) as well as the derived static margin (SM = $-C_{m_\alpha}/C_{L_\alpha}$). Table 4 summarises the three lateral-directional static stability coefficients (C_{l_β}, C_{Y_β}, and C_{n_β}). The static stability of the two CRMs is presented in the form of the relevant longitudinal and lateral force and moment coefficients, including the derivatives with respect to the angle of attack α and sideslip β wind angles. The latter quantities were calculated using a first-order central difference scheme, based on wind tunnel results with a sideslip delta of 2.5°. Figure 6 presents the roll, pitch, and yaw moment coefficient (C_l, C_m, C_n, respectively) trends with angle of attack at various airspeeds and zero sideslip for both CRMs. The lateral force and moment derivatives with respect to sideslip (C_{l_β}, C_{Y_β}, and C_{n_β}) are shown in Figure 7 for equivalent conditions. The following subsections detail the observed static stability trends for the longitudinal and lateral axes, respectively, in the context of the CRM geometries.

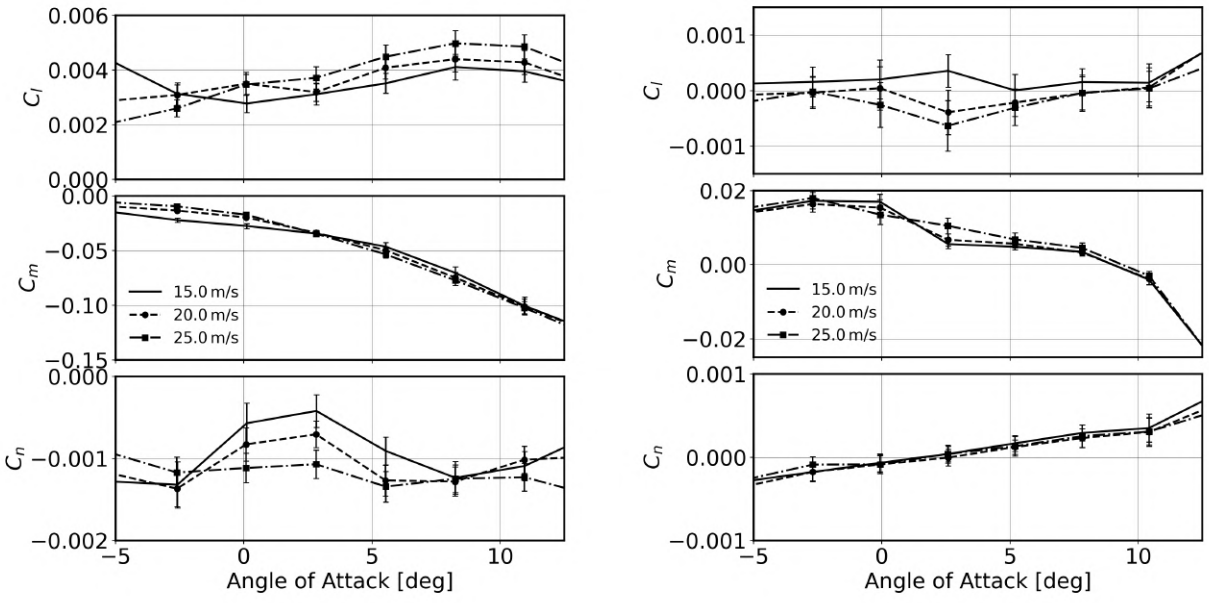
4.1 Longitudinal Stability: Opposing Reynolds Number Trends in the NT and NG

Both CRMs show a distinct and measurable variation in static margin with airspeed. For the NT, C_{m_α} becomes progressively more negative with increasing airspeed, from -0.130 at 15 m/s to -0.264 at 25 m/s, increasing the static margin from 3.1 % to 6.1 % MAC, respectively. The NG shows the opposite trend, with C_{m_α} becoming less negative from -0.127 to -0.082 across the same speed range, reducing the static margin from 3.5 % to 2.3 % MAC, respectively. The consistency of these trends

across repeated runs at each airspeed indicates they are physical rather than artifacts of measurement scatter. The underlying mechanism cannot be determined from force-balance data alone; surface-pressure measurements or flow visualisation would be required to attribute the trend to a Re-dependent boundary-layer state on the tail surfaces, wing camber effects, or fuselage interference. The lift-curve slopes of both CRMs are considerably lower than the theoretical 2π value for an infinite-span two-dimensional wing, with the measured C_{L_α} values being approximately 67 % and 58 % lower for the NT and NG configurations, respectively. This reduction is predominantly due to the low wing aspect ratios, which increase induced downwash and reduce the effective angle of attack experienced by the wing. The remaining deviation can be attributed to non-elliptic lift distributions and other three-dimensional viscous effects captured by the Oswald efficiency factor.

Table 3 – Summary of the key longitudinal-directional static stability parameters for both CRMs at various airspeeds. Standard deviations for experimental results are presented in-line as ($\pm$).

CRM	V [m/s]	C_{L_α}	C_{m_α}	SM [%]
NT	15.0	4.25 ($\pm$0.28)	-0.130 ($\pm$0.036)	3.1 ($\pm$0.9)
	17.5	4.20 ($\pm$0.24)	-0.167 ($\pm$0.029)	4.0 ($\pm$0.7)
	20.0	4.28 ($\pm$0.22)	-0.214 ($\pm$0.026)	5.0 ($\pm$0.7)
	22.5	4.31 ($\pm$0.21)	-0.244 ($\pm$0.024)	5.7 ($\pm$0.6)
	25.0	4.35 ($\pm$0.20)	-0.264 ($\pm$0.023)	6.1 ($\pm$0.6)
NG	15.0	3.64 ($\pm$0.23)	-0.127 ($\pm$0.027)	3.5 ($\pm$0.8)
	17.5	3.64 ($\pm$0.21)	-0.116 ($\pm$0.027)	3.2 ($\pm$0.8)
	20.0	3.62 ($\pm$0.19)	-0.105 ($\pm$0.030)	2.9 ($\pm$0.8)
	22.5	3.54 ($\pm$0.17)	-0.105 ($\pm$0.033)	3.0 ($\pm$0.9)
	25.0	3.50 ($\pm$0.16)	-0.082 ($\pm$0.033)	2.3 ($\pm$0.9)



(a) NT (b) NG

Figure 6 – Force-moment coefficients vs. angle of attack at various airspeeds for both CRMs.

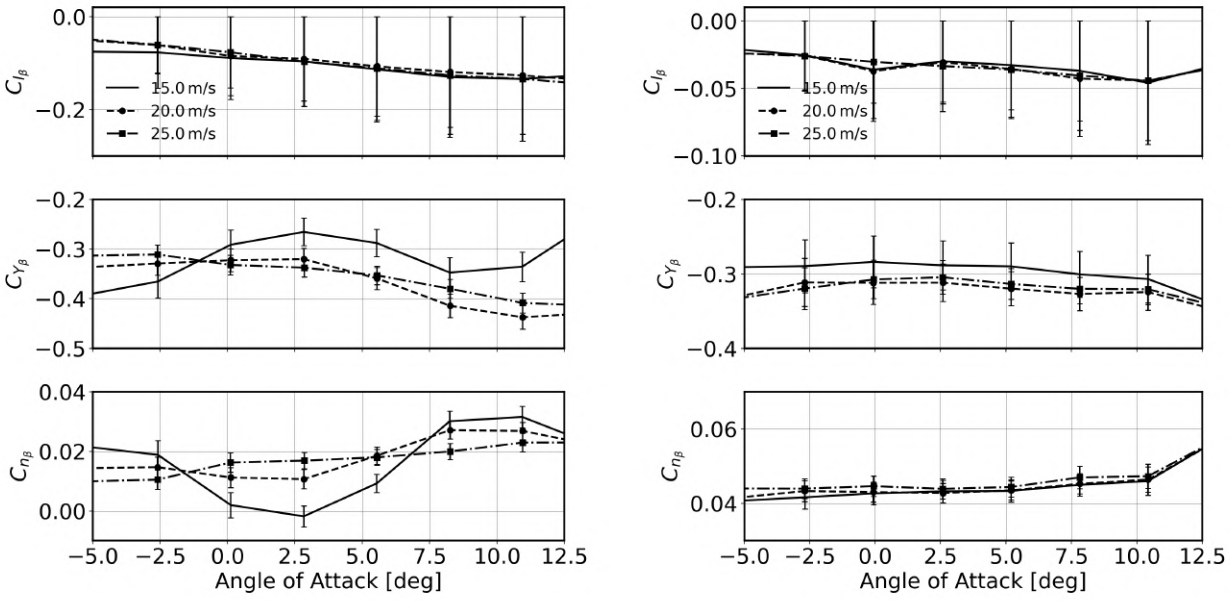
4.2 Lateral-directional Stability: Tail Geometry as the Governing Parameter

Both CRMs exhibit positive (restoring) lateral static stability, with negative values for the C_{l_β} and C_{Y_β} derivatives and positive values for the C_{n_β} terms. Nearly constant restoring side-force derivative values of $C_{Y_\beta} = -0.3$ across airspeed are observed for both the NT and NG, which lie within the lower

bound of the acceptable ranges for typical fixed-wing aircraft [20]. The NT exhibits a strong dependence of directional stability derivative on airspeed, with C_{n_β} increasing from 0.002 at 15 m/s to 0.016 at 25 m/s. The vertical fin has a mean chord of approximately 80 mm, giving a chord Reynolds number of roughly 80,000 at 15 m/s and 135,000 at 25 m/s. Across this range, laminar separation bubble behaviour governs fin surface effectiveness: at the lower Reynolds number, the bubble occupies a larger fraction of the chord. This reduces the effective lift-curve slope of the fin and its contribution to the restoring yaw moment. As airspeed increases, the bubble shortens, and fin effectiveness recovers. The NT remains flyable at 15 m/s with autopilot assistance, and the marginal C_{n_β} reflects the small fin area, which is significantly smaller than equivalent commercial FPV planes. The all-moving surface partially offsets the area reduction by recovering fin effectiveness relative to a conventional fixed-fin-and-rudder arrangement. Users of this dataset as a validation benchmark, should use the 25 m/s data as it provides the more meaningful test of directional stability prediction.

Table 4 – Summary of the lateral-directional static stability parameters for both CRMs at various airspeeds. Standard deviations for experimental results are presented in-line as (±).

CRM	V [m/s]	C_{l_β}	C_{Y_β}	C_{n_β}
NT	15.0	-0.089 (±0.008)	-0.291 (±0.030)	0.002 (±0.004)
	17.5	-0.095 (±0.008)	-0.306 (±0.025)	0.005 (±0.003)
	20.0	-0.085 (±0.008)	-0.322 (±0.023)	0.011 (±0.003)
	22.5	-0.093 (±0.008)	-0.329 (±0.021)	0.013 (±0.003)
	25.0	-0.077 (±0.007)	-0.332 (±0.020)	0.016 (±0.003)
NG	15.0	-0.036 (±0.007)	-0.284 (±0.035)	0.043 (±0.003)
	17.5	-0.039 (±0.007)	-0.312 (±0.031)	0.043 (±0.003)
	20.0	-0.037 (±0.007)	-0.312 (±0.029)	0.043 (±0.003)
	22.5	-0.034 (±0.006)	-0.315 (±0.026)	0.043 (±0.003)
	25.0	-0.030 (±0.006)	-0.307 (±0.026)	0.045 (±0.003)



(a) NT (b) NG

Figure 7 – Lateral force and moment derivatives with respect to sideslip trends at various airspeeds for both CRMs.

The NG C_{n_β} of 0.043 to 0.045 lies marginally above the minimum value of 0.04 rad^{-1} for adequate directional stability identified by Roskam [20]. In contrast to the NT, this derivative shows no mean-

ingful variation with airspeed. The fin has a root chord of 149 mm and a tip chord of 20 mm. The highly tapered planform concentrates fin area near the root, where the chord Reynolds number at 15 m/s is approximately 151,000. At this Reynolds number, laminar separation bubble effects on fin effectiveness are substantially reduced, and C_{n_β} is governed by fin geometry rather than Reynolds-number-dependent boundary layer state. The non-moving fin has no rudder and is the sole source of restoring moment for directional control. Systematic errors in fin effectiveness prediction of order 10 % are sufficient to shift an assessment of the tool for this configuration from adequate to inadequate directional stability. The NG, therefore, functions as a good stress test for directional stability prediction. Modelling choices that are inconsequential for the drag polar or longitudinal stability will produce qualitatively different conclusions about weathercock stability.

The factor-of-2.5 difference in C_{l_β} between the NT and NG is determined by where each configuration's tail surface area sits relative to the centre of gravity. Neither configuration has geometric dihedral or significant sweep, so the wing contribution to the dihedral effect is negligible for both. For the NT, both V-tail panels extend above the wing plane at 45° inclination. The fin of the NT, on the other hand, straddles the wing plane with equal area above and below. As a consequence, the NT V-tail generates a net side force in sideslip that acts above the CG and produces a rolling moment whose magnitude is proportional to the vertical distance between the tail aerodynamic centre and the roll axis. For the NG, the side forces from the upper and lower fin portions act in opposite directions about the roll axis and partially cancel, which reduces the net contribution. The high-wing mounting of the NT further increases C_{l_β} through fuselage-induced upwash on the windward panel, with no equivalent effect for the NG. The result is C_{l_β} of approximately -0.085 for the NT against -0.035 for the NG, a difference that simulation tools must reproduce at the geometry level rather than absorb into empirical corrections.

5. Conclusion

The NT and NG common research models establish the first openly available, geometrically reproducible aerodynamic and static stability dataset for sub-1 kg fixed-wing UAVs at chord Reynolds numbers of approximately 150,000 to 300,000. This is the regime where laminar separation bubbles dominate pressure recovery and where low-, mid-, and high-fidelity aerodynamic methods lack a shared calibration reference. These tool classes can now be evaluated on common ground: groups using different solvers on the same geometry will be able to attribute disagreement to modelling assumptions rather than platform differences.

Three contributions would complete the dataset for operational simulation validation. Flow visualisation using surface oil flow or particle image velocimetry would resolve the physical mechanisms driving the Reynolds-number-dependent stability trends identified in Section 4. This would allow connecting the integral force data to the boundary layer state and bubble location. Powered wind tunnel testing at matched advance ratios would characterise the propulsion-induced modifications to pitching moment and surface effectiveness, extending the dataset from the clean reference configuration to the powered flight condition. Flight testing of the printed CRM geometries with measured inertia properties would close the loop from the aerodynamic models to the full-vehicle dynamics, given that the open geometry is reproducible by any institution with access to rapid prototyping. Together, these extensions would establish the NT and NG as the basis for end-to-end validation of small UAV simulation tools, from aerodynamic coefficient prediction through to open- and closed-loop flight dynamics.

6. Contact Author Email Address

For further communication, please contact the corresponding author's email:
Juan Rasines Mazo, mailto: juan.rasinesmazo@sydney.edu.au

7. Copyright Statement

The authors confirm that they, and/or their company or organization, hold copyright on all of the original material included in this paper. The authors also confirm that they have obtained permission, from the copyright holder of any third party material included in this paper, to publish it as part of their paper. The authors confirm that

they give permission, or have obtained permission from the copyright holder of this paper, for the publication and distribution of this paper as part of the ICAS proceedings or as individual off-prints from the proceedings.

References

[1] V Schmitt. Pressure distributions on the onera m6-wing at transonic mach numbers, experimental data base for computer program assessment. *AGARD AR-138*, 1979.

[2] Melissa B Rivers. Nasa common research model: a history and future plans. In *AIAA Aviation 2019 Forum*, page 3725, 2019.

[3] John Vassberg, Mark Dehaan, Melissa Rivers, and Richard Wahls. Development of a common research model for applied cfd validation studies. In *26th AIAA applied aerodynamics conference*, page 6919, 2008.

[4] Michael A Frederick, Mark S Smith, Seung Y Yoo, Ryan Wallace, Jared C Duensing, Jeffrey A Housman, Karen A Deere, and Jeffrey K Viken. Development of the x-57 aerodynamic database. Technical report, National Aeronautics and Space Administration, 2025.

[5] PH Cabral, AP do Prado, E Carrera, A Pagani, A Racionero Sánchez-Majano, and M Enea. Aeroelastic tailoring based on virtually-generated allowables and high order finite elements for improved composite wing design. In *34th International Congress of the Aeronautical Science, ICAS-2024*, 2024.

[6] Gustavo HC Silva, Alex Pereira do Prado, Pedro Higino Cabral, Roeland De Breuker, and Johannes KS Dillinger. Tailoring of a composite regional jet wing using the slice and swap method. *Journal of Aircraft*, 56(3):990–1004, 2019.

[7] Nicholas K Borer. Flight performance estimates for the nasa x-57 distributed electric propulsion flight demonstrator. In *34th Congress of the International Council of the Aeronautical Sciences*, 2024.

[8] Ryan D Wallace, James R Reynolds, John D McMinn, and David Cox. Development of the x-57 mod iii/iv piloted simulator and discussion of the resultant flying qualities predictions. In *AIAA AVIATION FORUM AND ASCEND 2024*, page 4209, 2024.

[9] GK Ananda, PP Sukumar, and MS Selig. Measured aerodynamic characteristics of wings at low reynolds numbers. *Aerospace Science and Technology*, 42:392–406, 2015.

[10] Michael Selig. Low reynolds number airfoil design lecture notes. *VKI Lecture series*, 7:92, 2003.

[11] Shahfiq Shahjahan, Beau Emmerson, and Dries Verstraete. On the choice of turbulence model for the simulation of airfoils at reynolds numbers below 200,000. In *34th International Congress of the Aeronautical Science, ICAS-2024*, 2024.

[12] M Khalid and M Carbonaro. Low reynolds number aerodynamics on aircraft including applications in emerging uav technology. Technical report, RTO-AVT-VKI Lecture Series, von Karman Institute for Fluid Dynamics, Belgium . . . , 2003.

[13] Andrei Dorobantu, Austin Murch, Bérénice Mettler, and Gary Balas. System identification for small, low-cost, fixed-wing unmanned aircraft. *Journal of Aircraft*, 50(4):1117–1130, 2013.

[14] Bruce Owens, David Cox, and Eugene Morelli. Development of a low-cost sub-scale aircraft for flight research: The faser project. In *25th AIAA Aerodynamic Measurement Technology and Ground Testing Conference*, page 3306, 2006.

[15] Bogdan Løw-Hansen, Richard Hann, Kristoffer Gryte, Tor Arne Johansen, and Christoph Deiler. Modeling and identification of a small fixed-wing uav using estimated aerodynamic angles. *CEAS Aeronautical Journal*, pages 1–23, 2025.

[16] Dirk Reinhardt, Kristoffer Gryte, and Tor Arne Johansen. Modeling of the skywalker x8 fixed-wing uav: Flight tests and system identification. In *2022 International Conference on Unmanned Aircraft Systems (ICUAS)*, pages 506–515. IEEE, 2022.

[17] Jewel B Barlow, William H Rae, and Alan Pope. *Low-speed wind tunnel testing*. John wiley & sons, 1999.

[18] Beau Emmerson. *Post-Stall Performance of Cambered Airfoils*. PhD thesis, The University of Sydney, 2024.

[19] JCGM Jcgm et al. Evaluation of measurement data—guide to the expression of uncertainty in measurement. *Int. Organ. Stand. Geneva ISBN*, 50:134, 2008.

[20] Jan Roskam. *Airplane flight dynamics and automatic flight controls*. DARcorporation, 1998.